

High-Fidelity Two-Qubit Gates Using a Microelectromechanical-System-Based Beam Steering System for Individual Qubit Addressing

Ye Wang^{1,*}, Stephen Crain,¹ Chao Fang,¹ Bichen Zhang,¹ Shilin Huang¹, Qiyao Liang,²
Pak Hong Leung,² Kenneth R. Brown^{1,2,3,†} and Jungsang Kim^{1,4,‡}

¹*Department of Electrical and Computer Engineering, Duke University, Durham, North Carolina 27708, USA*

²*Department of Physics, Duke University, Durham, North Carolina 27708, USA*

³*Department of Chemistry, Duke University, Durham, North Carolina 27708, USA*

⁴*IonQ, Inc., College Park, Maryland 20740, USA*



(Received 7 April 2020; accepted 17 July 2020; published 6 October 2020)

In a large scale trapped atomic ion quantum computer, high-fidelity two-qubit gates need to be extended over all qubits with individual control. We realize and characterize high-fidelity two-qubit gates in a system with up to four ions using radial modes. The ions are individually addressed by two tightly focused beams steered using microelectromechanical system mirrors. We deduce a gate fidelity of 99.49(7)% in a two-ion chain and 99.30(6)% in a four-ion chain by applying a sequence of up to 21 two-qubit gates and measuring the final state fidelity. We characterize the residual errors and discuss methods to further improve the gate fidelity towards values that are compatible with fault-tolerant quantum computation.

DOI: [10.1103/PhysRevLett.125.150505](https://doi.org/10.1103/PhysRevLett.125.150505)

Trapped atomic ions are one of the leading qubit platforms for realizing a quantum computer due to long coherence times [1] and high-fidelity initialization, detection, and qubit gate operation [2–6]. The Mølmer-Sørensen (MS) gate [7,8] is a widely used two-qubit gate with demonstrated fidelities above 99.9% in two-ion systems utilizing axial modes [3,4]. For practical applications such as digital quantum simulation [9] and fault-tolerant quantum computation [10–12], the high-fidelity two-qubit gate needs to be extended to all qubits in the system with the ability to address individual qubits.

Individual addressing of atomic qubits in an array to realize qubit control has been accomplished by multichannel acousto-optic modulators [13,14], steering beams using acousto- or electro-optic modulators [15,16], and microelectromechanical system (MEMS) tilting mirrors [17,18]. For high-fidelity quantum logic gate operations in a larger array of qubits, one must consider loss of optical phase coherence between individual addressing beams and the crosstalk from an addressing beam to neighboring qubits that can impact the gate fidelity. Negligible crosstalk has been demonstrated using a MEMS-based individual addressing system [18], and gate schemes that are not sensitive to optical phase drift between the addressing beams have been developed [19–21] to overcome the fluctuation in optical beam paths among different beams.

Modulated pulse techniques are used to disentangle the internal qubit states from all collective motional modes and increase the robustness against frequency drifts. Amplitude-modulated (AM) gates [13,14,22,23], phase-modulated (PM) gates [24–26], multitone MS gates [27,28], and frequency-modulated (FM) gates [29–31]

have been developed and demonstrated. The fidelity of the AM, PM, and FM gates demonstrated in a chain of five (or more) ions is around 97%–98.5%, when radial motional modes are used for the gate [13,14,26,29,31]. Here, we develop the discrete FM gate, which is compatible with simple direct digital synthesizers (DDS).

With an optimized automatic calibration pipeline for the trapped ion system, we demonstrate high-fidelity two-qubit gates in a system with up to four ions using MEMS-based individual qubit addressing system. The two-qubit gate fidelity is 99.49(7)% in a two-ion chain and 99.30(6)% in a four-ion chain. The residual errors are analyzed and point to future directions for designing a high-fidelity two-qubit gate in longer ion chains.

The qubit is encoded in the hyperfine levels of the $^2S_{1/2}$ ground state manifold in a $^{171}\text{Yb}^+$ ion as $|0\rangle \equiv |F=0; m_F=0\rangle$ and $|1\rangle \equiv |F=1; m_F=0\rangle$ with a qubit frequency splitting of 12.642 821 GHz [32], as shown in Fig. 1(a). The qubit coherence time is measured to be more than 1 second using microwave single-qubit operations with a spin echo pulse. The qubit coherence time can be extended to more than 10 minutes using well-designed dynamical decoupling pulses [1]. The linear chain of $^{171}\text{Yb}^+$ ions are confined in a microfabricated linear radio frequency (rf) Paul trap [33] inside an ultra-high vacuum chamber. The two radial trap frequencies are $\nu_1 = 3.1$ MHz and $\nu_2 = 2.7$ MHz. The radial principal axes are rotated about 45° to the surface of the trap. The axial trap frequency is 600 and 150 kHz for two-ion and four-ion chains with $5\ \mu\text{m}$ ion spacing, respectively.

The qubits are laser cooled to near the ground state of the radial motional modes and initialized by optical pumping at

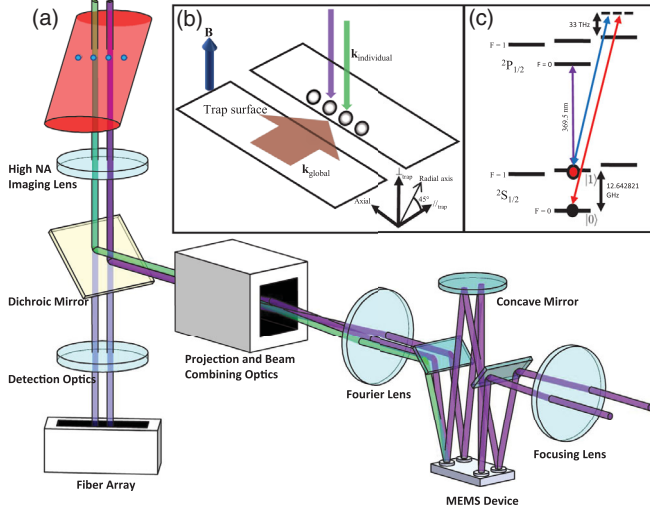


FIG. 1. (a),(b) Schematic representation of the Raman beam optical setup. The two individual addressing beams (purple) are steered by two pairs of mirrors tilting in orthogonal directions on a MEMS device to address any qubit in a chain (steered beam is shown in green). The trap axial axis is rotated by 45° with respect to both tilting axes of the MEMS mirrors to utilize orthogonal tilting mirrors in order to maximize the addressable qubits. The projection and beam combining optics are represented by a black box. (c) Energy level schematic of a $^{171}\text{Yb}^+$ ion. The red and blue lines indicate the two photon Raman transition for qubit operations.

the start of the experiment. This is followed by the qubit and motional manipulations, driven by stimulated Raman transitions using the beat note between two orthogonal beams generated from a mode-locked 355 nm picosecond-pulsed laser [34]. The qubits are then measured by state-dependent fluorescence. Photons scattered by each of the qubits are collected by a high numerical aperture lens ($\text{NA} \approx 0.6$) and coupled into individual multimode fibers in a fiber array and sent to separate detectors for individual qubit state detection, as shown in Fig. 1(c) [2]. Our scheme features negligible detection crosstalk at a level of 10^{-4} in state detection.

The optical setup for implementing Raman quantum gates is schematically illustrated in Figs. 1(a) and 1(b). One of the two orthogonal Raman beams is a global beam with an elliptical profile that illuminates all of the qubits simultaneously. The optical power and beam waist radius of the global beam are 40 mW and $8 \times 110 \mu\text{m}$. The other is a pair of tightly focused individual addressing beams which can be independently steered across the qubit chain using a MEMS device. Single-mode photonic crystal fibers are used to deliver the individual addressing beams to the beam-steering system and the global beam to beam-shaping optics [35]. We use acousto-optic modulators (AOMs) to control the frequency, phase and amplitude of all three beams prior to the fibers. Steering of each individual beam is accomplished by a pair of MEMS mirrors each tilting in

orthogonal directions. The details of the beam steering system is described in Ref. [18] and the Supplemental Material [36]. A dichroic mirror is used to reflect the Raman beams and transmit the qubit state-dependent fluorescence. The combination of single mode fiber and MEMS mirrors lead to clean Gaussian beams and low intensity crosstalk on the neighboring qubits at the level of 4×10^{-6} to 4×10^{-5} with a beam waist radius of $\sim 2.2 \mu\text{m}$ and an ion spacing of $\sim 5 \mu\text{m}$. The intensity crosstalk leads to a gate crosstalk, which is defined as the ratio of Rabi frequency between the target qubit and the neighboring qubit, at the level of 0.2% to 0.6%. The total number of addressable qubits is ~ 11 , limited by the maximum tilting angle of the MEMS mirrors. A maximum optical power of 10 mW, a safety limit to avoid degradation from the UV laser, is applied onto the MEMS mirror, which leads to 1.5 mW addressing beams going into the chamber and a maximum Rabi frequency for the motional sideband transition of 7 kHz.

Robust FM MS gates, using a continuous waveform generated by arbitrary waveform generator (AWG), have been demonstrated in a 5-qubit and 17-qubit ion chains [29,31]. To be compatible with DDS, the scheme is reconstituted to its discrete analog. The pulse is designed to be a sequence of equal-time segments, each of which has a constant frequency. The frequencies of the sequence are determined by a numerical optimizer, given the measured radial motional mode frequencies and a desired gate time as shown in Fig. 2(a). The optimizer generates a pulse sequence which closes the phase-space trajectories of all radial motional modes and therefore disentangles the spins and the motion, as shown in Fig. 2(b). It also constrains the Rabi frequency of the motional sideband transitions to be less than 7 kHz.

The detuning error, arising from the drift of motional mode frequencies, leads to unwanted spin-motion entanglement and deviation of the geometric phase for the MS evolution. The error from residual entanglement can be made negligible over ± 1 kHz detuning error ($< 2 \times 10^{-5}$) in the robust FM gate [29]. The accumulated phase deviation is represented by a deviation of the rotation angle of the gate, which can be considered as an amplitude error. In general amplitude errors are usually corrected for by tuning the laser intensity. However, if the detuning error changes on timescales faster than the time between calibration and the experimental circuit, then the intensity calibration is no longer accurate. Figure 2(c) shows the estimation of final-state fidelity after 1, 5, 13, and 21 consecutive MS gates are applied, as a function of detuning offset. The estimation considers both the residual spin-motion entanglement and the deviation of the rotation angle. Taking advantage of the negligible residual spin-motion entanglement against detuning errors in robust FM gates, one can introduce intentional detuning offset to precisely compensate for the small amplitude error.

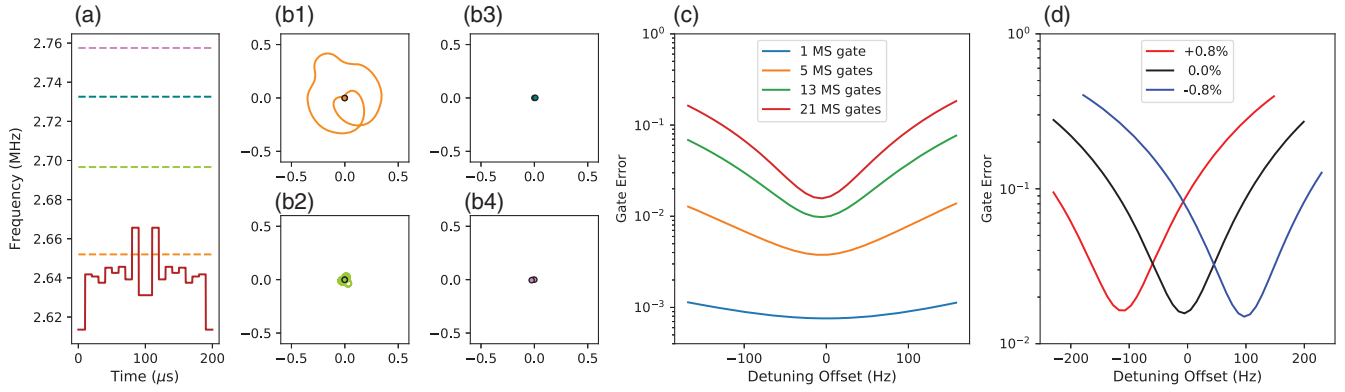


FIG. 2. (a) Discrete frequency modulation pulse sequence in the present experiment. The solution consists of 20 symmetric segments. The total gate time is $200 \mu\text{s}$. The required sideband Rabi frequencies are 5.55 and 5.47 kHz for FM gates in a two-ion chain and a four-ion chain. (b) Phase-space trajectory of four motional modes. (c) The estimated gross gate error of 1, 5, 13, 21 concatenated gates, given different detuning offsets. The estimation includes errors due to residual entanglement between spin and motion and the variation of the rotation angle. (d) The estimated of final-state error of 21 consecutive gates with $\pm 0.8\%$ deviation of Rabi frequency for the motional sideband transition. The amplitude error due to imperfect laser intensity can be compensated by intentional detuning offset.

As shown in Fig. 2(d), a ± 100 Hz detuning offset can compensate roughly $\mp 0.8\%$ deviation of Rabi frequency for the motional sideband transition.

We designed an automatic calibration process for all critical parameters. The rough calibration is performed every 30 minutes and takes ~ 10 minutes to complete. First, we calibrate the pointing accuracy of the two individual beams by tilting the MEMS mirror and observing the response of the target ion and neighboring ions to the beams. For each mirror, the tilt angle is calibrated by maximizing the population transfer of the target ion according to a single-qubit π rotation pulse and minimizing the those of the neighboring ions after a single-qubit 10π rotation pulse. Next, we address a single ion in the chain and measure all of the mode frequencies by scanning the beat-note frequency and observing the motional sideband transition. The discrete FM solution is calculated based on the measured mode frequencies and the predetermined gate time of $200 \mu\text{s}$. After loading the resulting pulse sequence to the random access memory of a field-programmable gate array; the field-programmable gate array then triggers the frequency updates for the DDS channels in real time during FM gates [40]. The beam power is calibrated by ensuring the population of target ion in the $|0\rangle$ state to be 0.5 after an expected 3.5π single-qubit rotation.

A final, fine calibration that takes tens of seconds is run just before the experiments to compensate for the small drift of the mode frequency and the laser intensity. As shown in Fig. 2(d), the small drift of the laser intensity can be compensated by introducing a detuning offset, which is a more precise method than tuning the laser intensity. This calibration is done by scanning the detuning offset with 21 concatenated gates applied to $|00\rangle$. The detuning at which $|00\rangle$ and $|11\rangle$ have equal probability indicates the perfect rotation angle for the MS gate. On the average, this

calibration improves our gate fidelity by about 0.5% compare to just doing the rough calibration.

We demonstrate the two-qubit MS gate in a two-ion chain and a four-ion chain. First, we initialize the target qubits to the $|00\rangle$ state and then apply a sequence of 1, 5, 13, and 21 MS gates to make the maximally entangled state $|\psi_+\rangle = (|00\rangle + i|11\rangle)/\sqrt{2}$. We then extract the state fidelity by measuring the population and the parity contrast [41]. The infidelity due to population leakage and the decrease of the parity contrast is plotted in the Fig. 3. The stochastic and the coherent error accumulate with concatenated gates in a linear and a quadratic way, respectively. However, the state preparation and measurement (SPAM) error remains constant. Using a linear fit for the data, we can extract the gate fidelity without the SPAM error. The two-qubit gate fidelity is 99.49(7)% in a two-ion chain, and 99.30(6)% in a four-ion chain. The data matches a linear fit, indicating that any coherent systematic error is negligible for the two-qubit gate in our system. The $\approx 2\%$ SPAM error consists of 1.24% preparation error and 0.98% detection error according to the single-qubit gate gate-set-tomography (GST) analysis [42] performed on the present system. The high SPAM error is due to the limited control bandwidth on DDSs and can be suppressed to less than 0.1% with an updated control system [43].

To understand the residual error for the two-qubit gate, we study the impact of various error sources on an ideal two-qubit gate using numerical simulation [3,4,8]. The simulated error budget is shown in Table I. Laser dephasing is the leading order effect. We use the optical phase-sensitive gate scheme [20] for our FM gates. This scheme leads to the sensitivities of the laser phase on our FM gates. We measure the laser coherence time with Ramsey interferometry using laser driven phase-sensitive single qubit operations. The Rabi frequency of this phase-

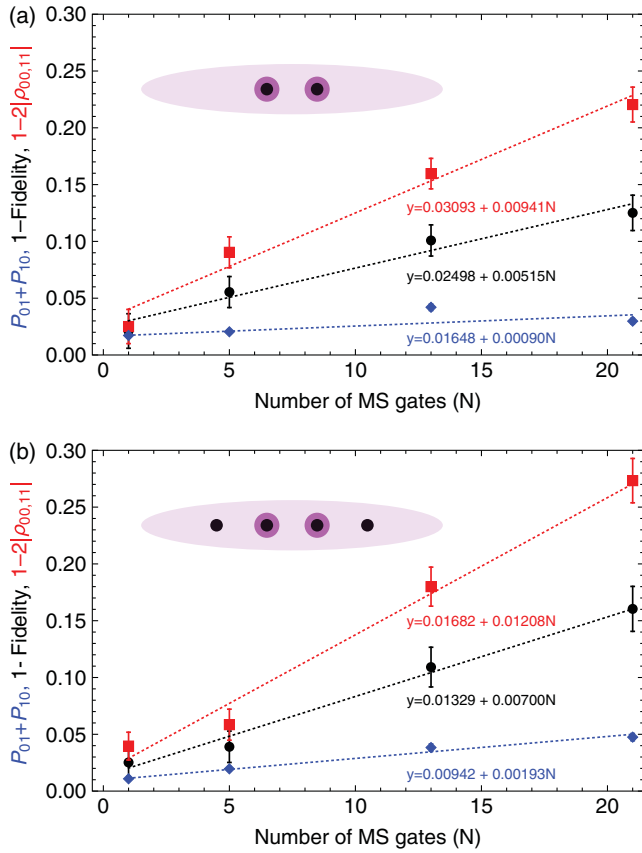


FIG. 3. Infidelity of the entangled state generated by repeated application of MS gates in a (a) two- and a (b) four-ion chain. The blue diamonds, red squares, and black circles are the population leakage to $|01\rangle$ and $|10\rangle$ space, the loss of parity contrast, and the infidelity of the final state, respectively.

sensitive operation is affected by motional states of radial modes, as describe by the Debye-Waller effect [8,44]. During the waiting time of Ramsey interferometry, the

motional state is heated from near ground state to a thermal state due to anomalous heating [45,46]. The heating rate of the center-of-mass mode and the tilt mode in the two-ion chain is measured to be ~ 200 and < 10 phonons/s, respectively. Therefore, the Ramsey contrast should be amended with the Debye-Waller effect. The corrected Ramsey contrast lead to laser coherence time of 83.3 ± 11.5 ms. On the other hand, the qubit coherence time is close to 1 second if we use microwave or laser driven phase-insensitive single-qubit operations for Ramsey interferometry. This significant reduction from 1 second to 83.3 ± 11.5 ms is caused by optical-phase fluctuations of two Raman beams at the qubit location arising from the variations of the optical path length.

Motional dephasing is the next significant source, and has many potential mechanisms [44]. In our system, it is mainly due to the amplitude fluctuation of the rf source used to generate the trapping potential. We apply a Ramsey interferometry to the motional sideband transition to measure the motional coherence time. To avoid the Debye-Waller effect, the measurement is done on the zigzag mode of a seven-ion chain, which features negligible anomalous heating. The motional coherence time is measured to be 36.3 ± 2.3 ms.

The intensity fluctuation of the tightly focused addressing Raman beams of $< 0.8\%$ is deduced by observing the decay of Rabi flopping for a phase-insensitive single qubit gate, driven by a co-propagating pair of Raman beams. The intensity fluctuation of the global beam should be at the same level. The upper bound of the off-resonant coupling to the carrier transition is estimated using the equation in Ref. [8].

The dominant error sources in our scheme are entirely technical in nature. The fluctuation of the Raman beam path and intensity can be suppressed by better optomechanical design. The noise from the rf source can be suppressed by

TABLE I. Mølmer-Sørensen gate Error budget. The errors are simulated with the full density matrix using the master equation including various error sources. The laser and motional coherence times is measured to be 83.3 ± 11.5 and 36.3 ± 2.3 ms, respectively. The beam intensity fluctuation is measured to be 0.8% . The motional heating rate of the center-of-mass mode and the tilt mode in two-ion chain is measured to be ~ 200 phonons/s and < 10 phonons/s, respectively.

Error source	Simulated error for four-ion chain	Simulated error for two-ion chain
	(10^{-3})	(10^{-3})
Laser dephasing	2.7 ± 0.4	2.7 ± 0.4
Motional dephasing	1.2 ± 0.1	1.1 ± 0.1
Raman beam intensity fluctuation	0.16	0.16
Off-resonant coupling	< 0.3	< 0.3
Motional heating	0.47	0.59
Spontaneous emission	< 0.25	< 0.25
FM Solution imperfection (due to laser power restriction)	0.76	0.04
Total	5.84 ± 0.5	5.14 ± 0.5

active feedback on the rf amplitude and better mechanical stability of the helical resonator. We observe UV-induced damage on the MEMS mirrors when the Raman beam power is increased to above 10 mW, so we increase the optical power of the global beam to maintain gate speeds under such power constraint on the individual beams. A faster gate will significantly suppress the error from laser and motional dephasing. The error due to spontaneous emission can be suppressed to be less than 1.7×10^{-4} by balancing global and addressing beam intensities. With the achievable laser coherence time (~ 1 s), motional coherence time (~ 0.5 s) [3], and negligible spontaneous emission rate [47], a two-qubit gate with fidelities well over 99.9% is possible in a long ion chain.

This work was primarily supported by the Office of the Director of National Intelligence—Intelligence Advanced Research Projects Activity through ARO Contract No. W911NF-16-1-0082 (experimental implementation), by DOE BES Award No. DE-SC0019449 (error analysis), by National Science Foundation Expeditions in Computing Award No. 1730104 (FM gate design), by National Science Foundation STAQ Project No. Phy-1818914 (simulation studies), and by DOE ASCR Award No. DE-SC0019294 (measurement protocol).

*ye.wang2@duke.edu

†ken.r.brown@duke.edu

‡jungsang.kim@duke.edu

- [1] Y. Wang, M. Um, J. Zhang, S. An, M. Lyu, J.-N. Zhang, L.-M. Duan, D. Yum, and K. Kim, *Nat. Photonics* **11**, 646 (2017).
- [2] S. Crain, C. Cahall, G. Vrijnsen, E. E. Wollman, M. D. Shaw, V. B. Verma, S. W. Nam, and J. Kim, *Commun. Phys.* **2**, 1 (2019).
- [3] C. J. Ballance, T. P. Harty, N. M. Linke, M. A. Sepiol, and D. M. Lucas, *Phys. Rev. Lett.* **117**, 060504 (2016).
- [4] J. P. Gaebler, T. R. Tan, Y. Lin, Y. Wan, R. Bowler, A. C. Keith, S. Glancy, K. Coakley, E. Knill, D. Leibfried *et al.*, *Phys. Rev. Lett.* **117**, 060505 (2016).
- [5] T. P. Harty, D. T. C. Allcock, C. J. Ballance, L. Guidoni, H. A. Janacek, N. M. Linke, D. N. Stacey, and D. M. Lucas, *Phys. Rev. Lett.* **113**, 220501 (2014).
- [6] J. Pino, J. Dreiling, C. Figgatt, J. Gaebler, S. Moses, C. Baldwin, M. Foss-Feig, D. Hayes, K. Mayer, C. Ryan-Anderson *et al.*, *arXiv:2003.01293*.
- [7] A. Sørensen and K. Mølmer, *Phys. Rev. Lett.* **82**, 1971 (1999).
- [8] A. Sørensen and K. Mølmer, *Phys. Rev. A* **62**, 022311 (2000).
- [9] B. P. Lanyon, C. Hempel, D. Nigg, M. Müller, R. Gerritsma, F. Zähringer, P. Schindler, J. T. Barreiro, M. Rambach, G. Kirchmair *et al.*, *Science* **334**, 57 (2011).
- [10] P. W. Shor, *Phys. Rev. A* **52**, R2493 (1995).
- [11] A. Y. Kitaev, *Ann. Phys. (Amsterdam)* **303**, 2 (2003).
- [12] D. Aharonov and M. Ben-Or, *SIAM J. Comput.* **38**, 1207 (2008).
- [13] S. Debnath, N. M. Linke, C. Figgatt, K. A. Landsman, K. Wright, and C. Monroe, *Nature (London)* **536**, 63 (2016).
- [14] K. Wright, K. Beck, S. Debnath, J. Amini, Y. Nam, N. Grzesiak, J.-S. Chen, N. Pisenti, M. Chmielewski, C. Collins *et al.*, *Nat. Commun.* **10**, 5464 (2019).
- [15] F. Schmidt-Kaler, H. Häffner, M. Riebe, S. Gulde, G. Lancaster, T. Deuschle, C. Becher, C. Roos, J. Eschner, and R. Blatt, *Nature (London)* **422**, 408 (2003).
- [16] D. D. Yavuz, P. B. Kulatunga, E. Urban, T. A. Johnson, N. Proite, T. Henage, T. G. Walker, and M. Saffman, *Phys. Rev. Lett.* **96**, 063001 (2006).
- [17] C. Knoernschild, X. L. Zhang, L. Isenhower, A. T. Gill, F. P. Lu, M. Saffman, and J. Kim, *Appl. Phys. Lett.* **97**, 134101 (2010).
- [18] S. Crain, E. Mount, S. Baek, and J. Kim, *Appl. Phys. Lett.* **105**, 181115 (2014).
- [19] P. J. Lee, K.-A. Brickman, L. Deslauriers, P. C. Haljan, L.-M. Duan, and C. Monroe, *J. Opt. B* **7**, S371 (2005).
- [20] I. V. Inlek, G. Vittorini, D. Hucul, C. Crocker, and C. Monroe, *Phys. Rev. A* **90**, 042316 (2014).
- [21] T. R. Tan, J. P. Gaebler, Y. Lin, Y. Wan, R. Bowler, D. Leibfried, and D. J. Wineland, *Nature (London)* **528**, 380 (2015).
- [22] S.-L. Zhu, C. Monroe, and L.-M. Duan, *Europhys. Lett.* **73**, 485 (2006).
- [23] C. F. Roos, *New J. Phys.* **10**, 013002 (2008).
- [24] T. J. Green and M. J. Biercuk, *Phys. Rev. Lett.* **114**, 120502 (2015).
- [25] A. R. Milne, C. L. Edmunds, C. Hempel, F. Roy, S. Mavadia, and M. J. Biercuk, *Phys. Rev. Applied* **13**, 024022 (2020).
- [26] Y. Lu, S. Zhang, K. Zhang, W. Chen, Y. Shen, J. Zhang, J.-N. Zhang, and K. Kim, *Nature (London)* **572**, 363 (2019).
- [27] Y. Shapira, R. Shaniv, T. Manovitz, N. Akerman, and R. Ozeri, *Phys. Rev. Lett.* **121**, 180502 (2018).
- [28] R. Blumel, N. Grzesiak, and Y. Nam, *arXiv:1905.09292*.
- [29] P. H. Leung, K. A. Landsman, C. Figgatt, N. M. Linke, C. Monroe, and K. R. Brown, *Phys. Rev. Lett.* **120**, 020501 (2018).
- [30] P. H. Leung and K. R. Brown, *Phys. Rev. A* **98**, 032318 (2018).
- [31] K. A. Landsman, Y. Wu, P. H. Leung, D. Zhu, N. M. Linke, K. R. Brown, L. Duan, and C. Monroe, *Phys. Rev. A* **100**, 022332 (2019).
- [32] S. Olmschenk, K. C. Younge, D. L. Moehring, D. N. Matsukevich, P. Maunz, and C. Monroe, *Phys. Rev. A* **76**, 052314 (2007).
- [33] P. L. W. Maunz, Sandia National Lab.(SNL-NM) Tech. Report No: SAND-2016-0796R 618951, 2016.
- [34] D. Hayes, D. N. Matsukevich, P. Maunz, D. Hucul, Q. Quraishi, S. Olmschenk, W. Campbell, J. Mizrahi, C. Senko, and C. Monroe, *Phys. Rev. Lett.* **104**, 140501 (2010).
- [35] Y. Colombe, D. H. Slichter, A. C. Wilson, D. Leibfried, and D. J. Wineland, *Opt. Express* **22**, 19783 (2014).
- [36] See the Supplemental Material at <http://link.aps.org/supplemental/10.1103/PhysRevLett.125.150505> for details of projection optics, the MS gate simulation, and the coherence time measurements, which includes Refs. [37–39].
- [37] D. L. Hayes, Ph. D. thesis, Joint Quantum Institute, University of Maryland, 2012, http://iontrap.umd.edu/wp-content/uploads/2013/10/Hayes_thesis.pdf.

- [38] G. Lindblad, *Commun. Math. Phys.* **48**, 119 (1976).
- [39] C. Gardiner, P. Zoller, and P. Zoller, *Quantum Noise: A Handbook of Markovian and Non-Markovian Quantum Stochastic Methods with Applications to Quantum Optics* (Springer Science & Business Media, New York, 2004).
- [40] E. Mount, D. Gaultney, G. Vrijsen, M. Adams, S.-Y. Baek, K. Hudek, L. Isabella, S. Crain, A. van Rynbach, P. Maunz *et al.*, *Quantum Inf. Process.* **15**, 5281 (2016).
- [41] D. Leibfried, B. DeMarco, V. Meyer, D. Lucas, M. Barrett, J. Britton, W. M. Itano, B. Jelenković, C. Langer, T. Rosenband *et al.*, *Nature (London)* **422**, 412 (2003).
- [42] R. Blume-Kohout, J. K. Gamble, E. Nielsen, K. Rudinger, J. Mizrahi, K. Fortier, and P. Maunz, *Nat. Commun.* **8**, 14485 (2017).
- [43] R. Noek, G. Vrijsen, D. Gaultney, E. Mount, T. Kim, P. Maunz, and J. Kim, *Opt. Lett.* **38**, 4735 (2013).
- [44] D. J. Wineland, C. Monroe, W. M. Itano, D. Leibfried, B. E. King, and D. M. Meekhof, *J. Res. Natl. Inst. Stand. Technol.* **103**, 259 (1998).
- [45] L. Deslauriers, S. Olmschenk, D. Stick, W. K. Hensinger, J. Sterk, and C. Monroe, *Phys. Rev. Lett.* **97**, 103007 (2006).
- [46] D. A. Hite, Y. Colombe, A. C. Wilson, K. R. Brown, U. Warring, R. Jördens, J. D. Jost, K. S. McKay, D. P. Pappas, D. Leibfried *et al.*, *Phys. Rev. Lett.* **109**, 103001 (2012).
- [47] R. Ozeri, W. M. Itano, R. Blakestad, J. Britton, J. Chiaverini, J. D. Jost, C. Langer, D. Leibfried, R. Reichle, S. Seidelin *et al.*, *Phys. Rev. A* **75**, 042329 (2007).